Journal of Applied Polymer Science

Micromechanical modeling of roll-to-roll processing of oriented polyethylene terephthalate films

M. Poluektov,[1,2,3] J. A. W. van Dommelen,[2] L. E. Govaert,[2] D. H. MacKerron,[4] M. G. D. Geers[2]

[1]Materials innovation institute (M2i), P.O. Box 5008, Delft, 2600 GA, The Netherlands

[2]Department of Mechanical Engineering, Eindhoven University of Technology, P.O. Box 513, Eindhoven, 5600 MB, The Netherlands

[3]Department of Information Technology, Uppsala University, Box 337, Uppsala, SE-751 05, Sweden

[4]DuPont Teijin Films UK, The Wilton Centre, Wilton, Redcar, TS10 4RF, United Kingdom

Correspondence to: J. A. W. van Dommelen (E-mail: J.A.W.v.Dommelen@tue.nl)

ABSTRACT: In this article, the thermo-mechanical time-dependent behavior of oriented polyethylene terephthalate (PET) films, which are used as a substrate material for flexible Organic Light-Emitting Diode (OLED)s, is analyzed. These films are subjected to conditions that are representative for the industrial manufacturing process. Effects of creep and thermal shrinkage are experimentally observed simultaneously. The aim of the article is to demonstrate the ability of the micromechanically-based model, which was previously used to separately describe both creep and thermal shrinkage of the polyethylene terephthalate film, to simulate experimentally observed anisotropic behavior of the film under complex loading conditions. This anisotropic behavior results from the microstructure, the internal stress state, and differences in constitutive behavior of the phases. © 2016 Wiley Periodicals, Inc. J. Appl. Polym. Sci. **2016**, *133*, 43384.

KEYWORDS: mechanical properties; properties and characterization; structure-property relations; theory and modeling

Received 1 September 2015; accepted 20 December 2015

DOI: 10.1002/app.43384

INTRODUCTION

The production of flexible electronics, such as OLEDs on flexible substrates, requires dimensionally highly stable polymer materials with a predictable mechanical response. The most commonly used materials are semicrystalline, oriented, and thermally stabilized polyethylene terephthalate (PET) and polyethylene naphthalate (PEN) films.[1,2] These films are produced by sequential biaxial stretching above the glass transition temperature, followed by cooling down to room temperature.[3] Subsequent heating of the films above the glass transition temperature leads to irreversible deformation under stress-free conditions, referred to as thermal shrinkage, or an emergence of shrinkage stress if the dimensions are fixed.[4–6] Such behavior can be classified as a shape-memory effect, where the partial recovery of the original shape is a result of the increased molecular mobility above the glass transition temperature, and whereby the driving force is due to the tendency of the structure to increase its entropy by relaxing the oriented conformation.[7] Moreover, tensile loading of the polymer substrate produces creep effects with a temperature-dependent creep rate. To ensure correct transistor patterning by subsequent industrial processing steps, it is necessary to precisely predict substrate deformation resulting from heating and loading. The behavior of these substrate materials is often described using phenomenological models, for example see Ref. 8. However, in this article, a multi-scale micromechanical model, which takes into account the two-phase nature of the semicrystalline material and molecular orientation, is applied to the oriented PET film. This allows to identify the nature of the material deformation from a micromechanical point of view.

Various constitutive models have been developed to simulate the macroscopic behavior of polymer materials, in particular for glassy polymers, such as the model of Buckley *et al.*,[9,10] Boyce and coworkers,[11,12] and Govaert and coworkers.[13,14] Following material characterization, they can describe complicated deformation cases, for example, flat-tip micro-indentation and notched impact tests,[15] the large-strain behavior of particle-reinforced composites with a polymer matrix[16] or strain localization and necking of tensile bars.[17] In the latter work, anisotropic flow was taken into account for modeling. In general, such models allow to incorporate thermo-rheologically complex behavior, through which they may also capture the response of semicrystalline polymers.[18] Even though it is possible to use orientation distribution functions as internal state variables to simulate the behavior of oriented semicrystalline polymers while tracking the evolution of morphology,[19] detailed conclusions

about microstructural changes, and local deformation mechanisms can only be obtained by using micromechanical or multi-scale simulations that have distinct constitutive descriptions of the underlying phases.

In micromechanical approaches, the material is assumed to consist of domains that have different properties, e.g. different orientations in the case of anisotropic material and/or different constitutive behavior in the case of a multi-phase material. Mean-field homogenization techniques are often used, since they are relatively computationally efficient. Among the most commonly used homogenization approaches are rules of mixtures (Voigt and Reuss schemes), the self-consistent scheme,[20] and the Mori-Tanaka scheme.[21] These homogenization methods can be directly applied to uniform domains, which consist of a single phase, or to complex domains, which are aggregates of several phases. There are many examples of these methods being used to estimate the elastic properties of semicrystalline polymers.[22–27] A number of micromechanical models are based on the self-consistent approach and successfully predict large plastic deformations in High-Density Polyethylene (HDPE)[28] and PET.[29] An alternative modeling approach, which is based on hybrid interaction schemes between Voigt and Reuss, is the so-called composite inclusion model.[30–33] It was developed to predict the elasto-plastic deformation and texture evolution of semicrystalline polymers. The crystalline and the amorphous phase of the material are described by dedicated constitutive relations. The two phases are assembled into a layered structure, the composite inclusion, which is the basic structural element of the model. The micromechanical approach is based on a hybrid interaction between these inclusions. The assembly could be either random, for instance, when isotropic material is modeled, or preferentially oriented.

To analyze the thermo-elasto-viscoplastic deformation of PET film, this article exploits the composite inclusion model.[31,32,34–36] Crystal plasticity is used as a constitutive model for the crystalline phase, with viscous slip on a limited number of slip systems. The non-crystalline phase is modeled with a glassy polymer model.[13,14] In Ref. 37, the tensile behavior of oriented polyethylene was modeled using the finite-element method where the material point behavior was obtained from the composite inclusion model. Experimentally observed effects were qualitatively captured by simulations. In Ref. 38, the composite inclusion model was used to describe the deformation kinetics of oriented HDPE and in Ref. 36, this model was extended with a pre-stretched amorphous phase to simulate short-term and long-term behavior of the oriented PET film taking into account pre-orientation. In Ref. 39, the constitutive behavior of the amorphous phase was further extended and reversible and irreversible thermal deformation of the PET was described.

In these previous studies, micromechanical models were used to predict the response of the material to relatively simple loading conditions. The goal of this work is to investigate the microstructure-dependent anisotropic response of PET films under complex loading conditions, particularly to analyze the response of PET film when subjected to industrially-relevant conditions, including heating from below to above the glass transition temperature and step-like loading and unloading, and compare experiments with simulations using the micromechanical model, which separately describes both creep and thermal shrinkage of polyethylene terephthalate film.[36,39] For the first time, a micromechanically-based model for the mechanical response of a semicrystalline polymer is evaluated for such complex loading conditions.

In this article, the film studied in Refs. 36 and 39 was subjected to complex thermo-mechanical loading and unloading. Thereafter, a film obtained with a similar manufacturing process was subjected to thermal stabilization and roll-to-roll processing steps and results were compared with the simulations. Two different films that were manufactured under similar conditions are used. The aim of the article is to demonstrate the ability of the microstructure-based model to describe strongly anisotropic behavior of the films as the result of their oriented microstructure, while neglecting low-order effects such as structural differences between the two films. A brief model description is given in the Model Description section, with a more extensive description and material parameters given in Appendices A–D.

MODEL DESCRIPTION

The constitutive behavior of semicrystalline material is modeled by an aggregate of two phase composite inclusions,[32,34] consisting of crystalline and amorphous domains, see also Appendix A. A microstructural elasto-viscoplastic constitutive model is defined for both the crystalline and the amorphous phase. The model is schematically illustrated in Figure 1.

The crystalline domain consists of regularly ordered molecular chains. The response of these domains is modeled elastically anisotropic combined with plastic deformation governed by crystallographic slip on a limited number of slip planes. A rate-dependent crystal plasticity model is used, for which the constitutive behavior of the slip systems is defined by the relation

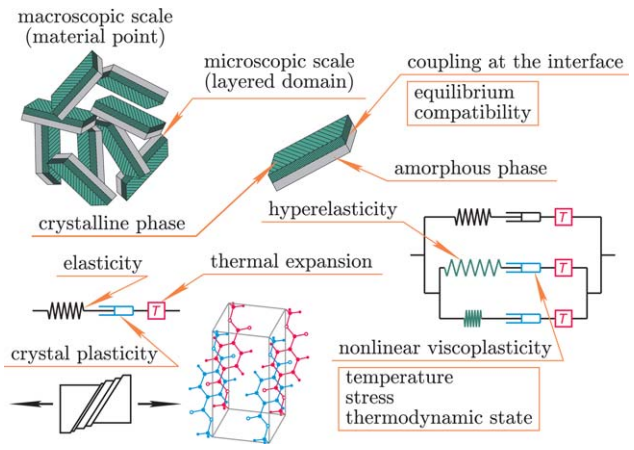

Figure 1. Schematic illustration of the two-phase micromechanical model used for semicrystalline polymer film.[32,34] Crystal plasticity and a glassy polymer model[13,14] are used for the constituent phases. [Color figure can be viewed in the online issue, which is available at wileyonlinelibrary.com.]

between the resolved shear stress and the resolved shear rate. This relation is referred to as the slip kinetics, for which an Eyring type relation is used, see Appendix B. For oriented films, a preferential orientation distribution based on X-ray diffraction measurements is used.

The amorphous domains are described with a constitutive model developed for glassy polymers, referred to as the Eindhoven Glassy Polymer (EGP) model,[13,14] which consists of a combination of viscoelastic Maxwell elements with neo-Hookean-like elasticity and a non-linear temperature and stress dependent viscosity, see Appendix C. The stress dependency is described using the Eyring flow model, whereas temperature dependency is modeled using the Arrhenius law. In this model, pre-stretching of the amorphous phase is incorporated for oriented films. The pre-deformation of the amorphous domains also drives irreversible deformation upon heating under stress-free conditions, also referred to as a shape memory effect. To simulate the behavior of the film at high temperatures and to model reversible and irreversible thermal deformation including the combination of thermal expansion and shrinkage as well as the effect of the heating rate, thermal expansion is incorporated in the micromechanical model for both phases, as well as a relaxation process for the internal pre-stress in the non-crystalline phase.

The mechanical behavior at the mesoscopic level is modeled by an aggregate of layered two-phase composite inclusions as proposed by Lee *et al.*[32] for rigid/viscoplastic materials. Each separate composite inclusion consists of a crystalline lamella, which is mechanically coupled to its corresponding amorphous layer. The stress and deformation fields within each phase are assumed to be piecewise homogeneous, however, they differ between the two coupled phases. The inclusion-averaged deformation gradient and the inclusion-averaged Cauchy stress are the volume-weighted averages of the respective phases. To relate the volume-averaged mechanical behavior of each composite inclusion to the imposed boundary conditions for an aggregate of inclusions, a hybrid local-global interaction law is used.[34]

A set of 100 inclusions was used in the simulations. The crystallographic orientations are shown in Figure 2. The microstructure of the PET film, which is used in the current study, was characterized in Ref. 36, where orientation distribution functions were obtained using Wide-Angle X-ray Diffraction (WAXD) and based on them a set of orientations was generated for the model. In biaxially stretched PET, crystals are oriented such that the (100) crystallographic planes are almost aligned with the plane of the film,[40] i.e., molecular chains are lying almost parallel to the film plane and benzene rings are at a small angle to the film surface. In the case of sequential biaxial stretching, the dominant chain orientation is machine direction (MD), as observed in Figure 2.

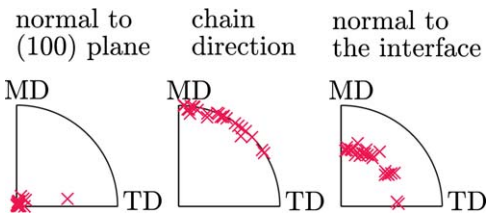

Figure 2. Equal area projection pole figures showing the initial crystallographic orientations (normal to the (100) plane and the [001] direction) and the normal to the interface between the phases ($\vec{n}^{I}$). The orientation set is taken from Ref. 36. [Color figure can be viewed in the online issue, which is available at wileyonlinelibrary.com.]

EXPERIMENTAL

Film Creep and Unloading

Thermally stabilized oriented PET film, manufactured by DuPont Teijin Films UK, was provided for the experimental analyses. The film was produced by sequential biaxial stretching with draw ratios $\lambda = 3.0$–3.5 in machine direction (MD) and transverse direction (TD). The film has an average thickness of 125 μm, a width of 90 cm, and an approximate crystallinity of 50%. The glass transition temperature of this material is $T_g \approx 70$°C.

True strain measurements at varying temperatures were performed under uniaxial tensile stress-controlled conditions using a Zwick Z010 universal tensile tester equipped with a video extensometer, a temperature controlled chamber and a 1 kN force cell. Samples were shaped according to ISO 527-2, type 1BA. Specific stress and temperature profiles were imposed. Prior to testing, the samples were dried in a temperature-controlled chamber at 50°C for 60 min to prevent interference of hygroscopic expansion with the measurements.

Three different cases were considered. In the first case, the influence of a variation of the creep stress on the material behavior above T_g was measured and modeled. Thereafter, a variation in temperature (heating from below T_g to above) was considered. In the third case, the effect of creep during heating was analyzed.

Creep and Unloading at Constant Temperature. The first test case is uniaxial creep under stress with a step-like drop. The time-dependence of the applied creep stress is shown in Figure 3. The creep stress of 5 MPa was maintained for 220 s and was reduced afterwards to 4, 3 or 1 MPa. A constant temperature of 90°C, which is above T_g, was maintained. Each sample was held at the test temperature for approximately 3 min before loading.

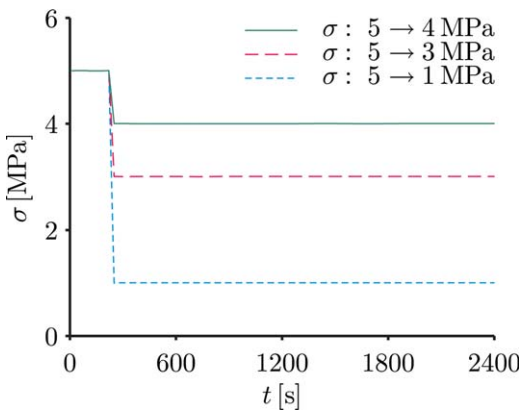

Figure 3. Temporal profile of the applied creep stress imposed in simulations and experiments. [Color figure can be viewed in the online issue, which is available at wileyonlinelibrary.com.]

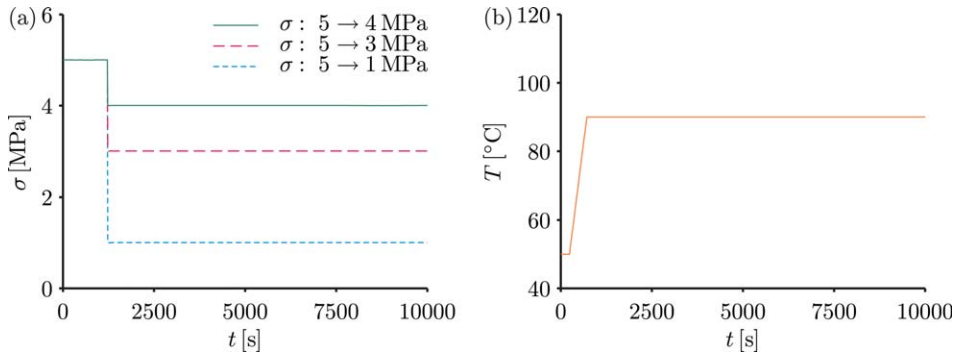

Figure 4. Temporal profile of the applied creep stress (a) and temperature (b) as imposed in the simulations and experiments. [Color figure can be viewed in the online issue, which is available at wileyonlinelibrary.com.]

Creep and Unloading with Heating above Glass Transition. In the second test case, the creep stress of 5 MPa was maintained for 1220 s and subsequently reduced to 4, 3 or 1 MPa. During the first stage of creep, after 240 s, the temperature was changed from 50°C to 90°C with a rate of 5°C/min, see Figure 4.

Creep during Heating. In the third test case, the material was heated from 35°C to 155°C (similar temperature range) under an applied stress of 1.5 MPa or 5 MPa. The heating was performed with a constant heating rate of 5°C/min.

Roll-to-Roll Film Processing

An experimental film of oriented polyethylene terephthalate (PET), also supplied by DuPont Teijin Films UK, was produced from PET polymer using a sequential biaxial stretching process and contained approximately 0.1% (vol.) of inert filler particles. The film process applied draw ratios $\lambda_{MD} = 3.2$ and $\lambda_{TD} = 3.4$ at temperatures of $T_{MD} = 80°C$ and $T_{MD} = 110°C$, respectively, and a 2% toe-in during a final heat setting treatment at 225°C. In a further process step, the film was stabilized via a heat treatment, where it was reheated to approximately 170°C under minimal tension (see Table I).

The film with dimensions 200 m × 410 mm × 125 μm, was further processed through a roll-to-roll barrier coater tool at Holst Centre (in Eindhoven, The Netherlands). No coating was applied and the film was simply collected after processing under two loading conditions. In this step, the film was heated to 130°C, subjected to a line tension of 100 N or 60 N, and subsequently cooled to room temperature. These line tensions correspond to a stress of 2.0 MPa and 1.2 MPa respectively.

The processed film was tested for dimensional stability using a shrinkage test based on ASTM D1204. In the test, a strip of the film was heated, without external constraints at 150°C for 30

Table I. Process Histories of the Samples Indicating the Temperature (°C), Time (s), and Stress (MPa) During Each Step

Sample group ID	Stabilization	Roll-to-roll processing	Shrinkage measurement
1	-	-	150°C, 30 min, 0 MPa
2	170°C, 180 s, 0.25 MPa	-	150°C, 30 min, 0 MPa
3	170°C, 180 s, 0.25 MPa	130°C → 30°C, 60 s, 1.2 MPa	150°C, 30 min, 0 MPa
4	170°C, 180 s, 0.25 MPa	130°C → 30°C, 60 s, 2.0 MPa	150°C, 30 min, 0 MPa

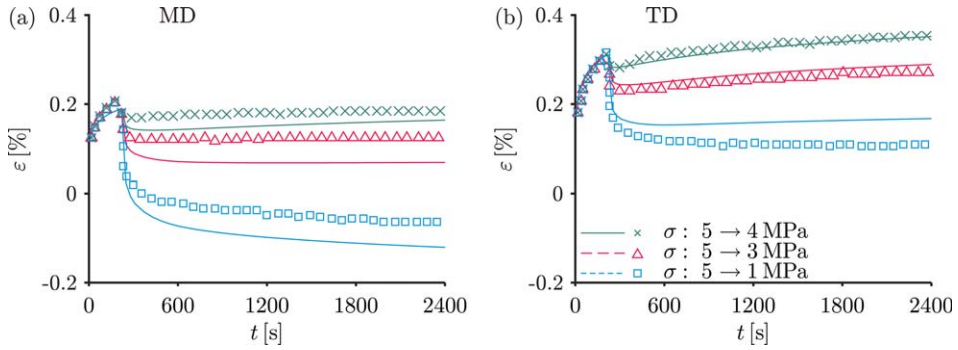

Figure 5. Time-dependence of strain in MD (a) and TD (b) under a creep stress of 5 MPa and subsequent unloading to 4 MPa, 3 MPa, and 1 MPa at 90°C; comparison of simulations (lines) and experiments (symbols). Each experimental curve corresponds to a single experiment. [Color figure can be viewed in the online issue, which is available at wileyonlinelibrary.com.]

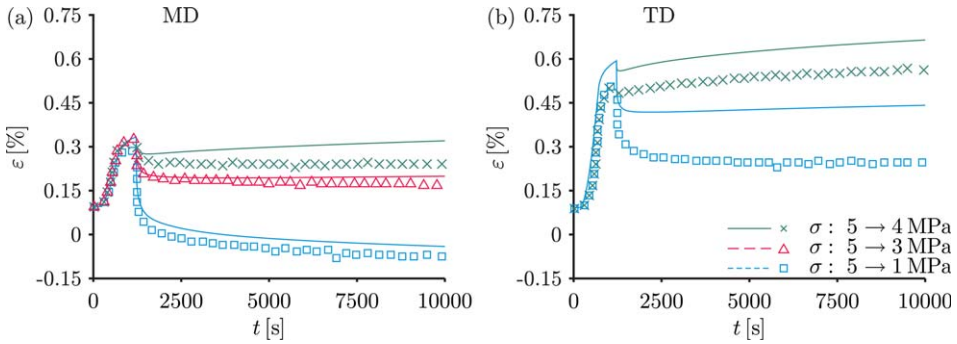

Figure 6. Time-dependence of strain in MD (a) and TD (b) under a creep stress of 5 MPa and subsequent unloading to 4 MPa, 3 MPa, and 1 MPa; comparison of simulations (lines) and experiments (symbols). Each experimental curve corresponds to a single experiment. During the first stage (creep stress of 5 MPa), the material is heated from 50°C to 90°C with a rate of 5°C/min. [Color figure can be viewed in the online issue, which is available at wileyonlinelibrary.com.]

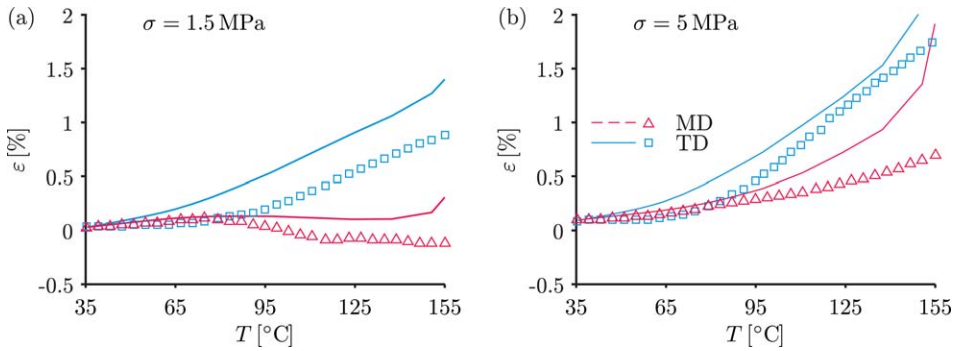

Figure 7. Temperature-dependence of strain in MD and TD during heating with an imposed heating rate of 5°C/min in the case of an applied creep stress of 1.5 MPa or 5 MPa; comparison of simulations (lines) and experiments (symbols). Each experimental curve corresponds to a single experiment. [Color figure can be viewed in the online issue, which is available at wileyonlinelibrary.com.]

min, cooled and re-examined for changes in length. Films at four stages of processing were used for shrinkage measurements: the original film as made at DuPont Teijin Films (DTF), Wilton; the film after stabilization; the film after stabilization and further roll-to-roll processing at 60 N; and the film after stabilization and further roll-to-roll processing at 100 N. The shrinkage measurement results are averages of three specimens. The processing history of the samples was summarized in Table I.

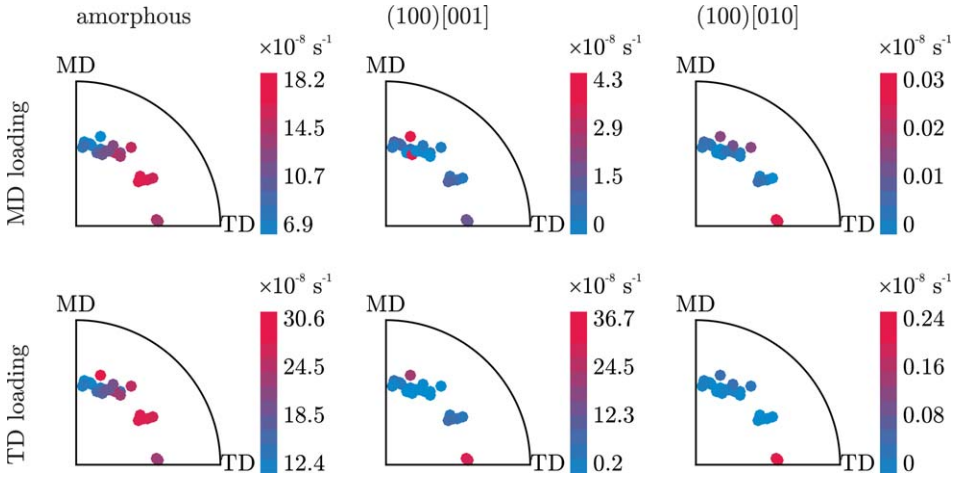

Figure 8. Equal area projection pole figures showing the initial interface normals between the phases ($\vec{n}^{I}$). Equivalent plastic deformation rate of the amorphous phase and plastic shear rates of the two most active slip systems of the crystalline phase are shown in color. Results corresponding to T=124°C are shown. The material is under MD and TD creep loading with an applied creep stress of 1.5 MPa, for which the macroscopic behavior is shown in Figure 7(a). [Color figure can be viewed in the online issue, which is available at wileyonlinelibrary.com.]

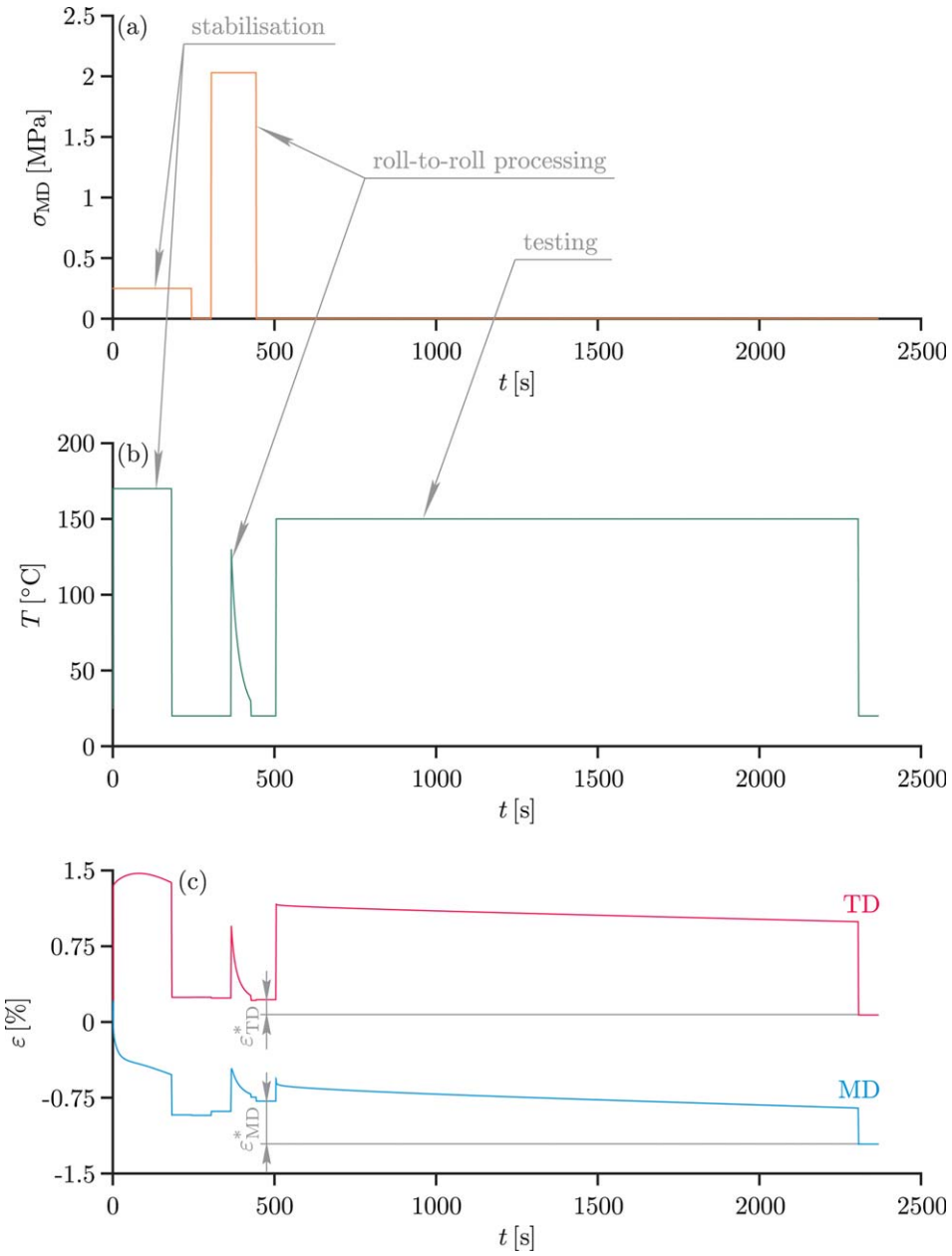

Figure 9. The imposed stress (a) and temperature (b) profiles for sample group 4, which were used in the model. Time-dependence of strain in MD and TD obtained with the model for sample group 4 (c); ε^*_{MD} and ε^*_{TD} are the strains observed in MD and TD, respectively, during shrinkage measurement. [Color figure can be viewed in the online issue, which is available at wileyonlinelibrary.com.]

RESULTS

Film Creep and Unloading

Creep and Unloading at Constant Temperature. The simulated film behavior qualitatively matches the measured behavior, as shown in Figure 5. In the case of MD loading, the strain increases further when the stress is reduced to 4 MPa, whereas it stays relatively constant when the stress drops to 3 MPa or decreases when the stress is lowered to 1 MPa. The constant strain in the case of a reduction to 3 MPa, is the result of a balance between the applied creep stress and the internal stress, which originates from the biaxial drawing of the film contributing to the deformation of the film above the glass transition temperature. After the instantaneous drop to 1 MPa, the strain becomes negative because of the internal stress. For MD, also large shrinkage was observed under stress-free conditions. In the case of TD loading, irreversible deformation above T_g is positive for this film.[39] Therefore, for the creep conditions imposed here, in the case of TD loading, only increasing or constant strains are observed, even for a stress reduction to 1 MPa.

In the case of MD loading, the micromechanical model overestimates the shrinkage strain by an approximate value of 0.06%

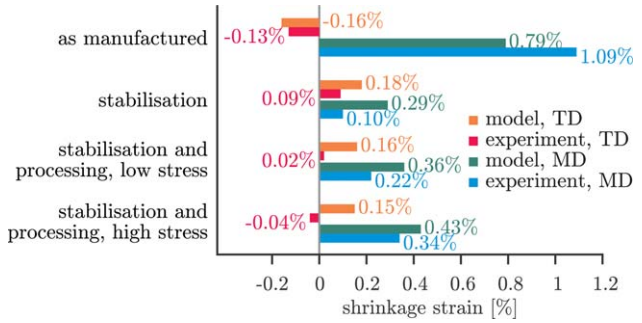

Figure 10. Irreversible thermal shrinkage, in simulations and measurements (positive values: shrinkage, negative values: expansion). [Color figure can be viewed in the online issue, which is available at wileyonlinelibrary.com.]

after unloading to 1 MPa. When material is loaded in TD, the predicted shrinkage strain is underestimated by a value of 0.06%. This is the result of the relatively high internal stress incorporated into the model, which is necessary to achieve a good match of stress-free shrinkage over a large temperature range.

Creep and Unloading with Heating above Glass Transition. Obviously, this is a more complicated case for modeling since here also thermal expansion of the crystalline and amorphous phases is activated. More details on creep during heating are provided in the next section. In this case, the simulated behavior also qualitatively matches the experimentally measured behavior, as shown in Figure 6. However, the model significantly overestimates the strain after unloading in TD to 1 MPa. In Ref. 39, it was observed that the proposed model overestimates the coefficient of thermal expansion (CTE) in TD for this film, which here induces an overestimation of the strain in the case of TD loading after heating. The deviation due to the thermal expansion appears during the first creep stage (creep stress of 5 MPa). The strain drop and subsequent deformation are predicted more accurately if this deviation in the thermal expansion is reduced, e.g., by introducing anisotropic thermal expansion of the non-crystalline phase in the model.

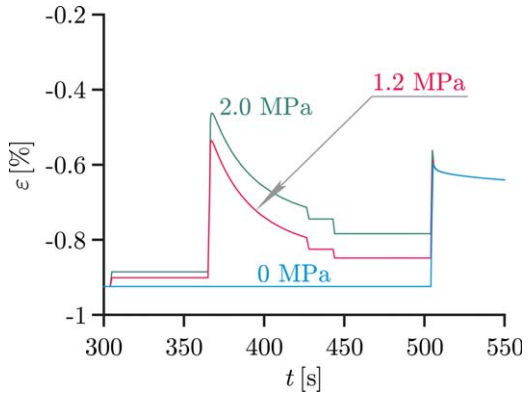

Figure 11. Time-dependence of strain in MD obtained with the model for sample group 2 (0 MPa), 3 (1.2 MPa), and 4 (2.0 MPa), during the roll-to-roll processing step and the beginning of the shrinkage testing step. [Color figure can be viewed in the online issue, which is available at wileyonlinelibrary.com.]

Note that a relatively large variation of thermal expansion was observed between measurements performed at identical conditions, i.e. thermal expansion due to heating was recorded to be $\Delta\varepsilon_T = 0.21\% \pm 0.05\%$ in MD. This is attributed to the intrinsic inhomogeneities in the orientation of the amorphous phase.

Creep during Heating. As observed in Figure 7, the rate of deformation (i.e., the slope) resulting from creep and the reversible and irreversible thermal deformations, is relatively well predicted by the model in the case of TD loading and somewhat overestimated in the case of MD loading. Overall, the results match qualitatively, although some quantitative mismatches persist. Similar to stress-free heating (see Ref. 39), the strain predicted by the model is higher than the measured strain. In the case of 5 MPa loading, above 110°C, the strain exceeds 1%, which is relatively large for the industrial application of interest (note that the material is not used under such conditions in practice).

In addition to the macroscopic behavior, the micromechanical model also describes deformations of separate phases. In Figure 8, the equivalent plastic deformation of the amorphous phase, defined as $\dot{\gamma}_p^a = \sqrt{2\boldsymbol{D}_{p_1}^a : \boldsymbol{D}_{p_1}^a}$, where $\boldsymbol{D}_{p_1}^a$ is the plastic part of the deformation rate in the first mode (see Appendix C), and absolute values of plastic shear rates of the (100)[001] chain slip system and the (100)[010] transverse slip system are shown with equal area projection pole figures. The second chain slip system, (010)[001], is almost inactive with a plastic deformation rate being several orders of magnitude lower than that of the other two slip systems. In Figure 8, results corresponding to only one temperature are shown, since the dependence of deformation rates on the layered domain orientation is qualitatively the same in the entire temperature range used in the creep loading simulations, shown in Figure 7. In the case of MD loading, plastic deformation of the material almost entirely results from plastic deformation of the amorphous phase. However, for the case of TD loading there is a significant contribution of (100)[001] chain slip. Layered domains with interface normals oriented close to TD demonstrate the highest shear rates on both slip systems. The dependence of the amorphous plastic deformation rate on the orientation of the interface is qualitatively similar for the cases of TD and MD creep loadings. Layered domains with interface normals approximately at 45° to TD appear to have the highest amorphous plastic deformation rate, i.e. the amorphous phase deforms mainly by shear. There is a quantitative difference between the plastic deformation rates in the cases of MD and TD loading. TD creep leads to a two times higher shear rate of the amorphous phase and almost an order of magnitude higher shear rate of the crystalline phase. This behavior of the constituent phases leads to a higher macroscopic creep rate in the case of TD loading, as seen in Figure 7(a).

Roll-to-Roll Film Processing

The composite inclusion model was used to simulate the film behavior during the processing steps described in Table I. In Refs. 36 and 39, identification of the model parameters was performed for a similar film, also manufactured at DuPont Teijin Films, Wilton. Since the manufacturing conditions of the films

are similar, these parameters (see Appendix D) are used for the simulations.

During the roll-to-roll processing step, the film is heated on a roll, yet without any deformation. After the film leaves the roll surface, at 130°C, it starts to deform under line tension, whereby the film immediately starts to cool by radiation. These conditions are simulated by applying a tensile stress in MD and instantaneous heating to 130°C with subsequent cooling according to the Stefan-Boltzmann law, where the film cools from 130°C to 30°C in 60 s.

In Figure 9, stress and temperature profiles that were used in the model for sample group 4 are shown. For sample group 3, the stress during the roll-to-roll processing step was 1.2 MPa and for sample group 2, this step was not applied. For sample group 1, both stabilization and roll-to-roll processing steps were not applied. The resulting shrinkage (ε^*_{MD} and ε^*_{TD}) was calculated using values before and after the shrinkage testing step, as shown in Figure 9(c). A comparison of the modeling results with the measurements is shown in Figure 10, where it is observed that thermal stabilization leads to a significant decrease of the shrinkage strain in MD and a change of irreversible deformation from expansion to shrinkage in TD, which is predicted by the model. For the roll-to-roll processed films, there is an increase of shrinkage strain with the increase of line tension during the processing step, which is also predicted by the micromechanical model. The region where the film is subjected to the roll-to-roll processing is separately shown in Figure 11, where the influence of different line tensions is demonstrated. The strain resulting from film creep during this step quickly disappears as soon as the film is re-heated (at the beginning of the shrinkage-testing step). Thermal shrinkage and creep become negligible when the film temperature falls below T_g (cooling from 130°C to 70°C takes about 18 s). There is only a minor influence of processing on the TD shrinkage, as seen in simulations and experiments, even though the model predicts slightly higher values.

The quantitative deviation of the modeling results from experiments may partly be due to different molecular orientations and internal stress states that are used in the model versus the real values in the experiments. The material parameters, which are used in the model, are obtained for the PET film with a slightly different manufacturing process. Hence, by using molecular orientations (crystal orientations), which are measured by WAXD for the considered film, and by fitting the internal stress state parameters, the model prediction might be improved.

CONCLUSIONS

In this article, a comparison of the thermomechanical behavior of oriented PET film under complex loading conditions obtained experimentally and computationally was performed, using the micromechanical composite inclusion model. This comparison demonstrates that the two-phase micromechanical model results are in adequate qualitative agreement with the experiment when the film is subjected to creep conditions, including step-like stress changes (film unloading), both below the glass transition temperature and above. The quantitative prediction of the anisotropic film behavior was made possible through the incorporation of the internal stress state of the amorphous phase (see also Ref. 39).

In the first part of the article, the same film as previously modeled, for which parameters were identified using simple loading cases (e.g., constant strain-rate and temperature stretching, tensile creep at constant stress and temperature, and stress-free heating), was subjected to combined thermo-mechanical loading and unloading. The largest deviations of simulated and measured results were observed during the heating stage, where in the case of MD loading the match between the experiments and the model is noticeably better than for TD loading. The main cause of this deviation is the difference between the measurements and predictions of the thermal expansion of the film. The model prediction of the CTE in MD is lower than in TD, whereas the opposite is observed experimentally. This was attributed to the oriented non-crystalline phase, which was modeled as an isotropic material with isotropic thermal expansion, whereas the addition of an anisotropic pre-stress state induces an anisotropic yield response. Overall, the simulated thermo-mechanical behavior qualitatively matches the measured behavior.

In the second part of the article, an industrially-relevant roll-to-roll process was considered. The model qualitatively predicts a large MD shrinkage strain of the thermally non-stabilized film and a small shrinkage strain of the stabilized film. Overall, the micromechanical model demonstrated the capability of simulating complex thermo-mechanical processing of the oriented semicrystalline polymer film based on the constitutive behavior of amorphous and crystalline phases of the material, their interconnection, and molecular orientation.

An advantage of the micromechanical model lies in its ability to predict the behavior of polymer films with various internal molecular orientations, assuming the behavior of the constituent phases is properly characterized. Another advantage is that local deformation mechanisms are recovered. Although the model is micromechanically-based, there are still some empirical parameters, such as the pre-deformation ratios, which should be determined from experimental data. The number of these parameters is relatively small, so the approach can be used to efficiently predict the behavior of films based on molecular orientation, although the requirement of microstructural characterization of the individual polymer films to obtain model parameters certainly imposes a limitation on the applicability of the approach.

APPENDIX A: COMPOSITE INCLUSION MODEL

In this section, the equations representing the composite inclusion model are summarized. A superscript "k" is introduced to indicate that a tensor or scalar describes an inclusion with number k. The constitutive equations for each phase of the N^I inclusions specify the stress depending on the deformation gradient in the following way:

$$\boldsymbol{\sigma}^{vk}(t) = \boldsymbol{\sigma}^{vk}\left(\boldsymbol{F}^{vk}, t^* | 0 \le t^* \le t\right); \quad k = \overline{1, N^I}; \quad v = \mathrm{a, c.} \qquad \text{(A1)}$$

The material is modeled as a collection of layered domains, referred to as inclusions. Inclusion averaged quantities are obtained as:

$$\boldsymbol{F}^{\mathrm{I}k}=(1-f_0)\boldsymbol{F}^{\mathrm{a}k}+f_0\boldsymbol{F}^{\mathrm{c}k}, \tag{A2}$$

$$\boldsymbol{\sigma}^{\mathrm{I}k}=\left(1-f^k\right)\ \boldsymbol{\sigma}^{\mathrm{a}k}+f^k\ \boldsymbol{\sigma}^{\mathrm{c}k}, \tag{A3}$$

where the volume fraction of the crystalline phase, with f_0 the initial value, is given by:

$$f^k=\frac{f_0 J^{\mathrm{c}k}}{(1-f_0)J^{\mathrm{a}k}+f_0 J^{\mathrm{c}k}}, \tag{A4}$$

with $J^{vk}=\det\left(\boldsymbol{F}^{vk}\right)$, $v=\mathrm{a},\mathrm{c}$. The orientation of the interface is given by two vectors $\vec{e}_1^{\,\mathrm{I}k}$ and $\vec{e}_2^{\,\mathrm{I}k}$ lying in the interface and its normal vector $\vec{e}_3^{\,\mathrm{I}k}=\vec{n}^{\mathrm{I}k}$. A subscript "0" indicates that quantities are taken in the initial configuration rather than in the current configuration.

In the inclusion, two layers are considered to be perfectly mechanically attached to each other. Therefore, equilibrium and compatibility conditions within each inclusion are enforced:

$$\boldsymbol{\sigma}^{\mathrm{c}k}\cdot\vec{e}_3^{\,\mathrm{I}k}=\ \boldsymbol{\sigma}^{\mathrm{a}k}\cdot\vec{e}_3^{\,\mathrm{I}k};\quad k=\overline{1,N^{\mathrm{I}}}; \tag{A5}$$

$$\boldsymbol{F}^{\mathrm{c}k}\cdot\vec{e}_{n0}^{\,\mathrm{I}k}=\boldsymbol{F}^{\mathrm{a}k}\cdot\vec{e}_{n0}^{\,\mathrm{I}k};\quad k=\overline{1,N^{\mathrm{I}}};\quad n=\{1,2\}. \tag{A6}$$

The $\hat{\boldsymbol{U}}$ interaction law between the inclusions is used,[34] for which an auxiliary deformation-like symmetric tensor $\hat{\boldsymbol{U}}$ is introduced as an unknown. A superscript "M" indicates quantities belonging to the macroscopic scale. The following interinclusion interaction laws are imposed:

$$\vec{e}_m^{\,\mathrm{I}k}\cdot\ \boldsymbol{\sigma}^{\mathrm{I}k}\cdot\vec{e}_n^{\,\mathrm{I}k}=\vec{e}_m^{\,\mathrm{I}k}\cdot\ \boldsymbol{\sigma}^{\mathrm{M}}\cdot\vec{e}_n^{\,\mathrm{I}k};\quad k=\overline{1,N^{\mathrm{I}}};\quad m,n=\{1,2\}; \tag{A7}$$

$$\boldsymbol{U}^{\mathrm{I}k}\cdot\vec{e}_{30}^{\,\mathrm{I}k}=\hat{\boldsymbol{U}}\cdot\vec{e}_{30}^{\,\mathrm{I}k};\quad k=\overline{1,N^{\mathrm{I}}}; \tag{A8}$$

$$\boldsymbol{R}^{\mathrm{I}k}=\boldsymbol{R}^{\mathrm{M}};\quad k=\overline{1,N^{\mathrm{I}}}, \tag{A9}$$

where the macroscopic Cauchy stress is determined by volume averaging:

$$\boldsymbol{\sigma}^{\mathrm{M}}=\sum_{k=1}^{N^{\mathrm{I}}}f^{\mathrm{I}k}\ \boldsymbol{\sigma}^{\mathrm{I}k}, \tag{A10}$$

and where $f^{\mathrm{I}k}=f_0^{\mathrm{I}k}J^{\mathrm{I}k}/J^{\mathrm{M}}$ is the volume fraction of the inclusion, $J^{\mathrm{M}}=\sum_{k=1}^{N^{\mathrm{I}}}f_0^{\mathrm{I}k}J^{\mathrm{I}k}$ is the macroscopic volume ratio, $f_0^{\mathrm{I}k}=1/N^{\mathrm{I}}$ is the initial volume fraction of the inclusion, and $J^{\mathrm{I}k}=\det\left(\boldsymbol{F}^{\mathrm{I}k}\right)$ is the volume change ratio of the inclusion. Volume averaging is also used to define the macroscopic right stretch tensor:

$$\left(\frac{J^{\mathrm{M}}}{J_\Sigma}\right)^{\frac{1}{3}}\boldsymbol{U}^{\mathrm{M}}=\sum_{k=1}^{N^{\mathrm{I}}}f_0^{\mathrm{I}k}\boldsymbol{U}^{\mathrm{I}k}; \tag{A11}$$

where $J_\Sigma=\det\left(\sum_{k=1}^{N^{\mathrm{I}}}f_0^{\mathrm{I}k}\boldsymbol{F}^{\mathrm{I}k}\right)$.

APPENDIX B: CONSTITUTIVE BEHAVIOUR OF THE CRYSTALLINE PHASE

In this section, the equations representing the constitutive behavior of the crystalline phase are summarized. A multiplicative decomposition of the deformation gradient tensor is used, i.e. $\boldsymbol{F}^{\mathrm{c}}=\boldsymbol{F}_{\mathrm{e}}^{\mathrm{c}}\cdot\boldsymbol{F}_{\mathrm{t}}^{\mathrm{c}}\cdot\boldsymbol{F}_{\mathrm{p}}^{\mathrm{c}}$, with $\boldsymbol{F}_{\mathrm{t}}^{\mathrm{c}}$ being the deformation gradient tensor resulting from thermal expansion.[41] The elastic behavior is modeled in the following way:

$$\boldsymbol{S}_{\mathrm{e}}^{\mathrm{c}}=\ {}^4\boldsymbol{\mathcal{C}}^{\mathrm{c}}:\boldsymbol{E}_{\mathrm{e}}^{\mathrm{c}}, \tag{B1}$$

where ${}^4\boldsymbol{\mathcal{C}}^{\mathrm{c}}$ is the elasticity tensor, $\boldsymbol{S}_{\mathrm{e}}^{\mathrm{c}}=J^{\mathrm{c}}\boldsymbol{F}_{\mathrm{e}}^{\mathrm{c}-1}\cdot\ \boldsymbol{\sigma}^{\mathrm{c}}\cdot\boldsymbol{F}_{\mathrm{e}}^{\mathrm{c}-\mathrm{T}}$ and $\boldsymbol{E}_{\mathrm{e}}^{\mathrm{c}}=\frac{1}{2}\left(\boldsymbol{F}_{\mathrm{e}}^{\mathrm{c}\mathrm{T}}\cdot\boldsymbol{F}_{\mathrm{e}}^{\mathrm{c}}-\boldsymbol{I}\right)$. The velocity gradient tensor due to thermal expansion is:

$$\boldsymbol{L}_{\mathrm{t}}^{\mathrm{c}}=\dot{\boldsymbol{F}}_{\mathrm{t}}^{\mathrm{c}}\cdot\boldsymbol{F}_{\mathrm{t}}^{\mathrm{c}-1}=\ \boldsymbol{\alpha}^{\mathrm{c}}\dot{T}, \tag{B2}$$

where $\boldsymbol{\alpha}^{\mathrm{c}}$ is a second-order tensor containing the thermal expansion coefficients. To complete the constitutive description, the viscoplastic behavior is defined through the plastic velocity gradient tensor:

$$\boldsymbol{L}_{\mathrm{p}}^{\mathrm{c}}=\dot{\boldsymbol{F}}_{\mathrm{p}}^{\mathrm{c}}\cdot\boldsymbol{F}_{\mathrm{p}}^{\mathrm{c}-1}=\sum_{\alpha=1}^{N^{\mathrm{s}}}\dot{\gamma}^{\alpha}\boldsymbol{P}_0^{\alpha}, \tag{B3}$$

where $\boldsymbol{P}_0^{\alpha}=\vec{s}_0^{\,\alpha}\vec{n}_0^{\,\alpha}$ is the non-symmetric Schmid tensor defined in the reference configuration. An Eyring flow rule is used for the plastic flow, i.e. the shear rate of slip system α is calculated in the following way:

$$\dot{\gamma}^{\alpha}=\xi^{\alpha}\exp\left(\frac{\Delta U^{\alpha}}{R}\left(\frac{1}{T_{\mathrm{r}}}-\frac{1}{T}\right)\right)\sinh\frac{\tau^{\alpha}}{\tau_0^{\alpha}}, \tag{B4}$$

where ΔU^{α} is the activation energy of the slip system, T is the current temperature, and T_{r} is a reference temperature. The shear stress τ^{α} on slip system α is defined as:

$$\tau^{\alpha}=\ \boldsymbol{\tau}^{\mathrm{c}}:\boldsymbol{P}^{\alpha};\quad \boldsymbol{P}^{\alpha}=\boldsymbol{F}_{\mathrm{e}}^{\mathrm{c}}\cdot\boldsymbol{P}_0^{\alpha}\cdot\boldsymbol{F}_{\mathrm{e}}^{\mathrm{c}-1};\quad \boldsymbol{\tau}^{\mathrm{c}}=J^{\mathrm{c}}\ \boldsymbol{\sigma}^{\mathrm{c}}. \tag{B5}$$

APPENDIX C: CONSTITUTIVE BEHAVIOUR OF THE AMORPHOUS PHASE

In this section, the equations representing the constitutive behavior of the non-crystalline phase are summarized. For each mode $i=\overline{1,N^{\mathrm{a}}}$, a multiplicative decomposition of the deformation gradient tensor is used (the plastic deformation is taken spin-free): $\boldsymbol{F}^{\mathrm{a}}=\boldsymbol{F}_{\mathrm{e}_i}^{\mathrm{a}}\cdot\boldsymbol{F}_{\mathrm{t}}^{\mathrm{a}}\cdot\boldsymbol{F}_{\mathrm{p}_i}^{\mathrm{a}}$. The Cauchy stress tensor is split into a driving stress, which, in turn, is split into a hydrostatic part, deviatoric part, and hardening stress:

$$\boldsymbol{\sigma}^{\mathrm{a}}=\ \boldsymbol{\sigma}_{\mathrm{s}}^{\mathrm{ah}}+\ \boldsymbol{\sigma}_{\mathrm{s}}^{\mathrm{ad}}+\ \boldsymbol{\sigma}_{\mathrm{r}}^{\mathrm{a}}. \tag{C1}$$

The driving stress represents the contribution of the intermolecular interactions and is modeled with N^{a} viscoplastic modes, whereas the hardening stress represents the molecular network modeled with N^{r} viscoplastic modes:

$$\boldsymbol{\sigma}_{\mathrm{s}}^{\mathrm{ah}}=K^{\mathrm{a}}\left(J_{\mathrm{e}}^{\mathrm{a}}-1\right)\boldsymbol{I};\quad \boldsymbol{\sigma}_{\mathrm{s}}^{\mathrm{ad}}=\sum_{i=1}^{N^{\mathrm{a}}}\boldsymbol{\sigma}_{\mathrm{s}_i}^{\mathrm{ad}}=\sum_{i=1}^{N^{\mathrm{a}}}G_i^{\mathrm{a}}\tilde{\boldsymbol{B}}_{\mathrm{e}_i}^{\mathrm{ad}};\quad \boldsymbol{\sigma}_{\mathrm{r}}^{\mathrm{a}}=\sum_{j=1}^{N^{\mathrm{r}}}G_{\mathrm{r}_j}\tilde{\boldsymbol{B}}_{\mathrm{er}_j}^{\mathrm{ad}}, \tag{C2}$$

with K^a being the bulk modulus, G_i^a the shear moduli, G_{r_j} the hardening moduli, and N^r the number of viscoelastic hardening modes. The isochoric elastic Finger tensor of mode i is calculated as:

$$\tilde{\boldsymbol{B}}_{e_i}^a = J_{e_i}^{a\,-\frac{2}{3}} \boldsymbol{F}_{e_i}^a \cdot \boldsymbol{F}_{e_i}^{aT}. \tag{C3}$$

The elastic deformation gradient tensors of the modes corresponding to the molecular network are determined from the following multiplicative decomposition:

$$\boldsymbol{F}^a = \boldsymbol{F}_{er_j}^a \cdot \boldsymbol{F}_t^a \cdot \boldsymbol{F}_{pr_j}^a \cdot \boldsymbol{F}_{d_j}^{a\,-1}, \quad j=\overline{1, N^r}, \tag{C4}$$

where $\boldsymbol{F}_{d_j}^a$ is a deformation gradient tensor determining the initial pre-deformation of the network, such that $\det\left(\boldsymbol{F}_{d_j}^a\right)=1$. In this article, the following form is adopted:

$$\boldsymbol{F}_{d_j}^a = \lambda_{TDj}\vec{e}_1\vec{e}_1 + \lambda_{MD_j}\vec{e}_2\vec{e}_2 + \frac{1}{\lambda_{TD_j}\lambda_{MD_j}}\vec{e}_3\vec{e}_3, \tag{C5}$$

where $\vec{e}_2$ corresponds to MD. The isochoric elastic Finger tensor of mode j, $\tilde{\boldsymbol{B}}_{er_j}^a$, is calculated in a similar way as in eq. (C3). The evolution of thermal expansion is given by

$$\boldsymbol{L}_t^c = \dot{\boldsymbol{F}}_t^c \cdot \boldsymbol{F}_t^{c\,-1} = \alpha^a \dot{T}\boldsymbol{I}, \tag{C6}$$

where α^a is the scalar isotropic thermal expansion coefficient.

The viscoplastic behavior is defined by the plastic part of the deformation rate:

$$\boldsymbol{D}_{p_i}^a = \frac{1}{2}\left(\boldsymbol{L}_{p_i}^a + \boldsymbol{L}_{p_i}^{a\,T}\right) = \frac{\boldsymbol{\sigma}_{s_i}^{a\,d}}{2\eta_i}. \tag{C7}$$

The viscosities η_i for $i=\overline{1, N^a}$ in eq. (C7) depend on the equivalent deviatoric driving stress τ, temperature T, and pressure p^a:

$$\eta_i = \eta_{0_i}\exp\left(\frac{\Delta U}{R}\left(\frac{1}{T}-\frac{1}{T_r}\right)\right)\frac{\tau/\tau_0}{\sinh(\tau/\tau_0)}\exp\left(\frac{\mu p^a}{\tau_0}\right), \quad i=\overline{1, N^a}; \tag{C8}$$

$$\tau = \sqrt{\frac{1}{2}\,\boldsymbol{\sigma}_s^{a\,d} : \boldsymbol{\sigma}_s^{a\,d}}; \quad \tau_0 = \frac{kT}{V^*}, \quad p^a = -\frac{1}{3}\mathrm{tr}\left(\sigma_s^{a\,h}\right) \tag{C9}$$

where R is the universal gas constant, ΔU the activation energy, T_r a reference temperature, $\boldsymbol{\sigma}_s^{a\,d}$ is the overall deviatoric driving stress, k is the Boltzmann constant, and V^* the activation volume. The plastic part of the deformation rate corresponding to the molecular network, $\boldsymbol{D}_{er_j}^a$, is calculated in a similar way as in eq. (C7). The viscosities η_{r_j} for hardening modes are only temperature dependent:

$$\eta_{r_j} = \eta_{0r_j}\exp\left(\frac{\Delta U_{r_j}}{R}\left(\frac{1}{T}-\frac{1}{T_r}\right)\right), \quad j=\overline{1, N^r}. \tag{C10}$$

APPENDIX D: MODEL PARAMETERS

The stiffness matrix of the PET crystal is temperature dependent. In the model, values interpolated at a particular temperature are used.[42] Here, only values at ambient temperature

Table DI. Components of the Stiffness Tensor and Thermal Expansion Tensor of the PET Crystal at 300 K, From Ref. 42

Parameter	C_{11}^c	C_{22}^c	C_{33}^c	C_{44}^c	C_{55}^c	C_{66}^c	C_{12}^c	C_{13}^c	C_{23}^c	C_{14}^c	C_{24}^c
Value (GPa)	14.4	17.3	178.0	6.6	1.4	1.2	6.4	3.4	9.5	−2.2	3.3
Parameter	C_{34}^c	C_{15}^c	C_{25}^c	C_{35}^c	C_{45}^c	C_{16}^c	C_{26}^c	C_{36}^c	C_{46}^c	C_{56}^c	
Value (GPa)	3.8	−0.3	−0.5	−0.7	0.2	−1.8	0.5	−1.8	−0.4	0.0	
		Parameter	α_{11}^c	α_{22}^c	α_{33}^c	$2\alpha_{23}^c$	$2\alpha_{13}^c$	$2\alpha_{12}^c$			
		Value (10^{-5} K^{-1})	11.4	4.12	−1.07	4.5	−1.38	5.05			

Table DII. Reference Shear Rates at Different Temperatures for the PET Crystal

Slip system	(100)[001]	(010)[001]	(100)[010]
ξ^α at 295 K (s^{-1})	10^{-16}	10^{-80}	10^{-30}
ξ^α at 463 K (s^{-1})	8×10^{-6}	7×10^{-7}	2×10^{-2}

Table DIII. Model Parameters for PET, Non-Crystalline Phase

		Parameter	ΔU (kJ/mol)	V^* (nm^3)	α^a (K^{-1})	T_r (K)	K^a (MPa)	μ[-]				
		Value	230	3.24	$7 \cdot 10^{-5}$	323	1800	0.048				
Parameter	ζ_1	ζ_2	ζ_3	ζ_4	ζ_5	ζ_6	ζ_7	ζ_8	ζ_9	ζ_{10}	ζ_{r_1}	ζ_{r_2}
Value (s)	10^{12}	10^{11}	10^{10}	10^9	10^8	10^7	10^6	10^5	10^4	10^3	10^{13}	10^{13}
Parameter	G_1^a	G_2^a	G_3^a	G_4^a	G_5^a	G_6^a	G_7^a	G_8^a	G_9^a	G_{10}^a	G_{r_1}	G_{r_2}
Value (MPa)	8	13	12	16	50	53	102	257	274	28	2.35	2.35
		Parameter	λ_{TD1}[-]	λ_{MD1}[-]	λ_{TD2}[-]	λ_{MD2}[-]	ΔU_{r_1} [kJ/mol]	ΔU_{r_2} [kJ/mol]				
		Value	1.37	0.93	0.39	1.74	225	245				

(300 K) are listed in Table DII, where the Voigt notation (11, 22, 33, 23, 31, 12) is used (the coordinate system $\vec{i}_1\vec{i}_2\vec{i}_3$ is coupled to the crystal, see Refs. 36 and 42). Parameters for the viscoplastic deformation of the crystalline phase are listed in Table DII. For all slip systems, the reference shear stress is $\tau_0^\alpha = 1.1$ MPa.

For the non-crystalline phase, values of the parameters can be found in Table DIII. Relaxation times $\zeta = \eta/G^a$ for the rejuvenated state are listed instead of viscosities.

ACKNOWLEDGMENTS

This research was carried out under project number M62.2.09331 in the framework of the Research Program of the Materials innovation institute (M2i) (www.m2i.nl). DuPont Teijin Films (www.dupontteijinfilms.com) and Holst Centre (www.holstcentre.com) are gratefully acknowledged for supplying the materials for this research. This research has been partially supported by the European Union through the Seventh Framework Programme (FP7-ICT-2012, project number 314362). The authors also wish to thank W. Manders and J. Evans for processing the PET film and subsequent measurements.

REFERENCES

1. MacDonald, W. A.; Looney, M. K.; MacKerron, D.; Eveson, R.; Adam, R.; Hashimoto, K.; Rakos, K. *J. Soc. Inf. Disp.* **2007**, *15*, 1075.
2. MacDonald, W. A. *Polymer Int.* **2008**, *57*, 672.
3. Jones, D. P.; MacKerron, D. H.; Norval, S. V. *Plast. Rubber Compos.* **2013**, *42*, 66.
4. Haworth, B.; Dong, Z. W.; Davidson, P. *Polymer Int.* **1993**, *32*, 325.
5. Göschel, U. *Polymer* **1996**, *37*, 4049.
6. Schoukens, G.; Samyn, P.; Maddens, S.; van Audenaerde, T. *J. Appl. Polymer Sci.* **2003**, *87*, 1462.
7. Heuchel, M.; Sauter, T.; Kratz, K.; Lendlein, A. *J. Polymer Sci. B: Polymer Phys.* **2013**, *51*, 621.
8. Barink, M.; van den Berg, D.; Yakimets, I.; Giesen, P.; van Dommelen, J. A. W.; Meinders, E. *Microelectron. Eng.* **2011**, *88*, 999.
9. Buckley, C. P.; Jones, D. C. *Polymer* **1995**, *36*, 3301.
10. Buckley, C. P.; Dooling, P. J.; Harding, J.; Ruiz, C. *J. Mech. Phys. Solid.* **2004**, *52*, 2355.
11. Boyce, M. C.; Parks, D. M.; Argon, A. S. *Mech. Mater.* **1988**, *7*, 15.
12. Arruda, E. M.; Boyce, M. C. *Int. J. Plast.* **1993**, *9*, 697.
13. Govaert, L. E.; Timmermans, P. H. M.; Brekelmans, W. A. M. *J. Eng. Mater. Technol.* **2000**, *122*, 177.
14. Klompen, E. T. J.; Engels, T. A. P.; Govaert, L. E.; Meijer, H. E. H. *Macromolecules* **2005**, *38*, 6997.
15. van Breemen, L. C. A.; Klompen, E. T. J.; Govaert, L. E.; Meijer, H. E. H. *J. Mech. Phys. Solid.* **2011**, *59*, 2191.
16. Figiel, L.; Dunne, F. P. E.; Buckley, C. P. *Model. Simulat. Mater. Sci. Eng.* **2010**, *18*, 015001.
17. Li, H. X.; Buckley, C. P. *Int. J. Plast.* **2010**, *26*, 1726.
18. van Breemen, L. C. A.; Engels, T. A. P.; Klompen, E. T. J.; Senden, D. J. A.; Govaert, L. E. *J. Polymer Sci. B: Polymer Phys.* **2012**, *50*, 1757.
19. Shepherd, J. E.; McDowell, D. L.; Jacob, K. I. *J. Mech. Phys. Solid* **2006**, *54*, 467.
20. Hill, R. *J. Mech. Phys. Solid.* **1965**, *13*, 213.
21. Benveniste, Y. *Mech. Mater.* **1987**, *6*, 147.
22. Guan, X.; Pitchumani, R. *Polymer Eng. Sci.* **2004**, *44*, 433.
23. Bedoui, F.; Diani, J.; Regnier, G. *Polymer* **2004**, *45*, 2433.
24. Bedoui, F.; Diani, J.; Regnier, G.; Seiler, W. *Acta Mater.* **2006**, *54*, 1513.
25. Ahzi, S.; Bahlouli, N.; Makradi, A.; Belouettar, S. *J. Mech. Mater. Struct.* **2007**, *2*, 1.
26. Gueguen, O.; Ahzi, S.; Belouettar, S.; Makradi, A. *Polymer Sci.* **2008**, *50*, 523.
27. Gueguen, O.; Ahzi, S.; Makradi, A.; Belouettar, S. *Mech. Mater.* **2010**, *42*, 1.
28. Nikolov, S.; Lebensohn, R. A.; Raabe, D. *J. Mech. Phys. Solid.* **2006**, *54*, 1350.
29. Makradi, A.; Ahzi, S.; Gregory, R. V.; Edie, D. D. *Int. J. Plast.* **2005**, *21*, 741.
30. Parks, D. M.; Ahzi, S. *J. Mech. Phys. Solid.* **1990**, *38*, 701.
31. Lee, B. J.; Argon, A. S.; Parks, D. M.; Ahzi, S.; Bartczak, Z. *Polymer* **1993**, *34*, 3555.
32. Lee, B. J.; Parks, D. M.; Ahzi, S. *J. Mech. Phys. Solid.* **1993**, *41*, 1651.
33. Ahzi, S.; Lee, B. J.; Asaro, R. J. *Mater. Sci. Eng A* **1994**, *189*, 35.
34. van Dommelen, J. A. W.; Parks, D. M.; Boyce, M. C.; Brekelmans, W. A. M.; Baaijens, F. P. T. *J. Mech. Phys. Solid.* **2003**, *51*, 519.
35. Sedighiamiri, A.; Govaert, L. E.; Kanters, M. J. W.; van Dommelen, J. A. W. *J. Polymer Sci. B: Polymer Phys.* **2012**, *50*, 1664.
36. Poluektov, M.; van Dommelen, J. A. W.; Govaert, L. E.; Geers, M. G. D. *Model. Simulat. Mater. Sci. Eng.* **2014**, *22*, 055024.
37. van Dommelen, J. A. W.; Schrauwen, B. A. G.; van Breemen, L. C. A.; Govaert, L. E. *J. Polymer Sci. B: Polymer Phys.* **2004**, *42*, 2983.
38. Sedighiamiri, A.; Senden, D. J. A.; Tranchida, D.; Govaert, L. E.; van Dommelen, J. A. W. *Comput. Mater. Sci.* **2014**, *82*, 415.
39. Poluektov, M.; van Dommelen, J. A. W.; Govaert, L. E.; Geers, M. G. D. *Comput. Mater. Sci.* **2015**, *98*, 189.
40. Bin, Y. Z.; Oishi, K.; Yoshida, K.; Nakashima, T.; Matsuo, M. *Polymer J.* **2004**, *36*, 394.
41. van Dommelen, J. A. W.; Parks, D. M.; Boyce, M. C.; Brekelmans, W. A. M.; Baaijens, F. P. T. Micromechanical Modeling of the Thermo-Elasto-Viscoplastic Behavior of Semi-Crystalline Polymers, In Proceedings of the European Congress on Computational Methods in Applied Sciences and Engineering, Barcelona, **2000**.
42. Rutledge, G. C. *Macromolecules* **1997**, *30*, 2785.